# Quantitative Assessment of Boiling Histotripsy Progression Based on Color Doppler Measurements

Minho Song, *Graduate Student Member, IEEE*, Gilles P. L. Thomas, Vera A. Khokhlova, Oleg A. Sapozhnikov, Michael R. Bailey, Adam D. Maxwell, Petr V. Yuldashev, and Tatiana D. Khokhlova, *Member, IEEE*

***Abstract*— Boiling histotripsy (BH) is a mechanical tissue liquefaction method that uses sequences of millisecond-long high intensity focused ultrasound (HIFU) pulses with shock fronts. The BH treatment generates bubbles that move within the sonicated volume due to acoustic radiation force. Since the velocity of the bubbles and tissue debris is expected to depend on the lesion size and liquefaction completeness, it could provide a quantitative metric of the treatment progression. In this study, the motion of bubble remnants and tissue debris immediately following BH pulses was investigated using high-pulse repetition frequency (PRF) plane-wave color Doppler ultrasound in ex vivo myocardium tissue. A 256-element 1.5 MHz spiral HIFU array with a coaxially integrated ultrasound imaging probe (ATL P4-2) produced 10 ms BH pulses to form volumetric lesions with electronic beam steering. Prior to performing volumetric BH treatments, the motion of intact myocardium tissue and anticoagulated bovine blood following isolated BH pulses was assessed as two limiting cases. In the liquid blood the velocity of BH-induced streaming at the focus reached over 200 cm/s, whereas the intact tissue was observed to move toward the HIFU array consistent with elastic rebound of tissue. Over the course of volumetric BH treatments tissue motion at the focus locations was dependent on the axial size of the forming lesion relative to the corresponding size of the HIFU focal area. For axially small lesions, the maximum velocity after the BH pulse was directed toward the HIFU transducer and monotonically increased over time from about 20–100 cm/s as liquefaction progressed, then saturated when tissue was fully liquefied. For larger lesions obtained by merging multiple smaller lesions in the axial direction, the high-speed streaming away from the HIFU transducer was observed at the point of full liquefaction. Based on these observations, the maximum directional velocity and its location along the HIFU propagation axis were proposed and evaluated as candidate metrics of BH treatment completeness.**

***Index Terms*— Boiling histotripsy (BH), color Doppler, high intensity focused ultrasound (HIFU), quantification method.**

## I. Introduction

BOILING histotripsy (BH) is a noninvasive tissue liquefaction technique that uses sequences of millisecond-long high-intensity focused ultrasound (HIFU) pulses with shock fronts [1]. High-amplitude shocks formed in the focal region of the HIFU beam due to nonlinear propagation effects play an essential role in the BH method by enhancing the localized heating at the beam focus that results in reaching boiling temperature within milliseconds and formation of a millimeter (mm)-sized vapor cavity in tissue [2]. Interaction of the incident shocks with the vapor cavity enables tissue fractionation mechanisms such as atomization, microfountain [3], [4], and the formation of a prefocal cavitation cloud [5]. As a result of BH treatment, soft tissue at the focus is transformed into a liquid lesion filled with subcellular debris. Connective tissue structures, such as blood vessels, ducts, and organ capsules, have been found to be more resistant to BH ablation than cellular tissue, thus providing an additional margin of safety [6]. Sharp borders and negligible thermal effects are characteristics of BH lesions. Because of these beneficial attributes, BH is being developed for a wide range of clinical applications [7], such as liver, pancreas, and kidney tumor ablation [8], [9], liquefaction of large hematomas for fine-needle aspiration [10], and potentiating antitumor immune response [9], [11].

Manuscript received 26 May 2022; accepted 29 September 2022. Date of publication 5 October 2022; date of current version 28 November 2022. This work was supported in part by NIH under Grant R01EB007643, and Grant R01GM122859, Grant R01EB025187, Grant R01EB023910; and in part by RSF under Grant 20-12-00145. *(Corresponding author: Minho Song.)*

Minho Song is with the Department of Mechanical Engineering, University of Washington, Seattle, WA 98195 USA (e-mail: songmh@uw.edu).

Gilles P. L. Thomas is with the Center for Industrial and Medical Ultrasound, Applied Physics Laboratory, University of Washington, Seattle, WA 98195 USA.

Vera A. Khokhlova and Oleg A. Sapozhnikov are with the Center for Industrial and Medical Ultrasound, Applied Physics Laboratory, University of Washington, Seattle, WA 98195 USA, and also with the Physics Faculty, Moscow State University, 119991 Moscow, Russia.

Michael R. Bailey is with the Department of Mechanical Engineering, University of Washington, Seattle, WA 98195 USA, also with the Center for Industrial and Medical Ultrasound, Applied Physics Laboratory, University of Washington, Seattle, WA 98195 USA, and also with the Department of Urology, School of Medicine, University of Washington, Seattle, WA 98195 USA.

Adam D. Maxwell is with the Center for Industrial and Medical Ultrasound, Applied Physics Laboratory, University of Washington, Seattle, WA 98195 USA, and also with the Department of Urology, School of Medicine, University of Washington, Seattle, WA 98195 USA.

Petr V. Yuldashev is with the Physics Faculty, Moscow State University, 119991 Moscow, Russia.

Tatiana D. Khokhlova is with the Division of Gastroenterology, School of Medicine, University of Washington, Seattle, WA 98195 USA.

This article has supplementary downloadable material available at https://doi.org/10.1109/TUFFC.2022.3212266, provided by the authors.

Digital Object Identifier 10.1109/TUFFC.2022.3212266

To date, BH ablation has primarily utilized ultrasound imaging and sensing for real-time treatment planning, guidance, and evaluation of treatment outcomes, although MRI imaging has been explored as well [12], [13]. Coaxial B-mode imaging offers excellent qualitative guidance in real-time [1], [8] due to the fact that mm-sized vapor bubbles and micrometer ($\mu$m)-sized cavitation bubbles mediating the treatment appear as hyperechoic regions [14], [15]. Conversely, as tissue loses structure in the course of the treatment, the lesion progressively becomes hypoechoic. In addition, B-mode imaging provides a practical way to determine the HIFU output level necessary for inducing boiling by detecting the formation of the hyperechoic region when the BH pulse amplitude is gradually increased. Various ultrasound sensing methods have also been used to detect boiling and cavitation bubble activity in BH sonication. In particular, fluctuation of the input voltage on a single-element HIFU transducer was used to determine the initiation of boiling [1], [2], [12]. Passive cavitation detection (PCD), prevalently used in many other cavitation-based ultrasound therapies, gives another option for treatment planning and monitoring [2], [16].

Although coaxial B-mode ultrasound provides a means for BH planning, targeting, and real-time feedback on treatment progression, the information on treatment completeness is only qualitative. Having a quantitative metric of the degree of tissue fractionation obtained in real time during the treatment is important because tissues have inherently variable sensitivities to BH fractionation, depending on their mechanical properties, structure, and composition [7]. As a result, different tissue types, even within the same targeted volume, require different treatment duration (or the number of BH pulses of a certain frequency, duration, and shock amplitude delivered per focus location) for complete fractionation [8]. For example, in volumetric BH treatments of in vivo porcine kidneys, the number of pulses required for full liquefaction was largest for the collecting system, smaller for the medulla, and smaller yet for the cortex [8]. The use of the same BH treatment duration in all targets could lead to overtreatment and excessively long treatment time or undertreatment. Thus, a real-time ultrasound-based strategy that would provide spatially resolved, quantitative information on the degree of tissue liquefaction is needed.

Although a quantitative liquefaction metric for BH is yet to be developed, several candidate metrics and methods have been investigated for other histotripsy regimes—shock-scattering histotripsy and microtripsy [17]. These histotripsy techniques use shorter pulses than BH (microseconds rather than milliseconds) and higher in situ pressure levels to engage different cavitation regimes and arrive at mechanical tissue ablation. In early studies, B-mode ultrasound backscatter signal intensity from liquefied lesions was quantified over the course of shock-scattering histotripsy treatment and correlated with the degree of tissue liquefaction [18]. This metric decayed exponentially with treatment time because subcellular debris and liquefied tissue are less scattering than intact tissue [19]; however, the trend became less obvious toward the end of the treatment, when the tissue within the lesion became almost fully liquefied, making it difficult to determine treatment completion. In another method, Young's modulus of the treated tissue was measured using shear wave elastography [20], and peak-to-peak tissue displacement using acoustic radiation force impulse-induced shear wave was correlated with the tissue damage [21]. These two shear wave methods were based on the hypothesis that the tissue stiffness will be gradually reduced with liquefaction. Even though this metric outperformed the backscatter intensity for assessing tissue damage, using it for interrogating large volumes of liquefied tissue would be challenging since shear waves do not propagate through a liquid. Further, liquefaction indicators derived from passive cavitation imaging (PCI) or sensing have also been explored in phantoms and ex vivo tissue [22], [23]. PCI was shown to provide a more sensitive measure of tissue liquefaction compared to B-mode, although with limited axial resolution.

Another method of cavitation-induced tissue damage assessment was termed bubble-induced color Doppler (BCD). In BCD, each HIFU pulse is followed by a color Doppler ensemble to elicit the acoustic responses of and/or detect the dissolution of the residual bubbles. Thus, BCD is a sensitive means to detect the presence of bubbles and potentially evaluate their size based on the dynamics of their dissolution [24]. In the context of microtripsy, where a very short HIFU pulse is used to generate a large contiguous bubble at the focus, its expansion, collapse, and subsequent surrounding tissue motion are affected by the amount of liquid around the bubble; thus, it could serve as metric for tissue liquefaction. According to the studies using BCD in cavitation-cloud histotripsy [25], [26], [27], the spatially averaged velocity over the cavitation cloud area is directed away from the HIFU transducer immediately after the pulse, and then tissue rebounds in the opposite direction in about 10 ms. It was reported that the time when the rebound velocity reaches its peak increases and then saturates as the tissue is liquefied.

In this article, BCD was applied to BH with the goal of developing quantitative metrics of tissue liquefaction based on the observations of the motion of bubbles and tissue debris within the lesion following BH pulses. Compared to cavitation cloud histotripsy, a single BH pulse is much longer and expected to transfer a much higher momentum to the tissue at the focus. Bubble dynamics and distribution following each BH pulse are also different: relatively large bubbles are slowly dissolving (rather than collapsing) and are distributed throughout the lesion [1]. With these considerations, we hypothesize that the bubbles and tissue debris will move within the liquefied lesion due to HIFU radiation force at progressively higher velocity as the tissue is more liquefied. This Doppler-measured velocity could then serve as a quantitative metric of tissue liquefaction. To test this hypothesis, the following experiments were performed. First, anticoagulated bovine blood and intact bovine myocardium were considered as the limiting cases of fully liquefied and fully intact tissue, correspondingly. The tissue motion induced by BH pulses of varying amplitudes was investigated experimentally using high pulse repetition frequency (PRF) color Doppler. Then, volumetric BH treatments of different duration were performed in the bovine myocardium, and the resulting lesions were bisected and evaluated grossly for size

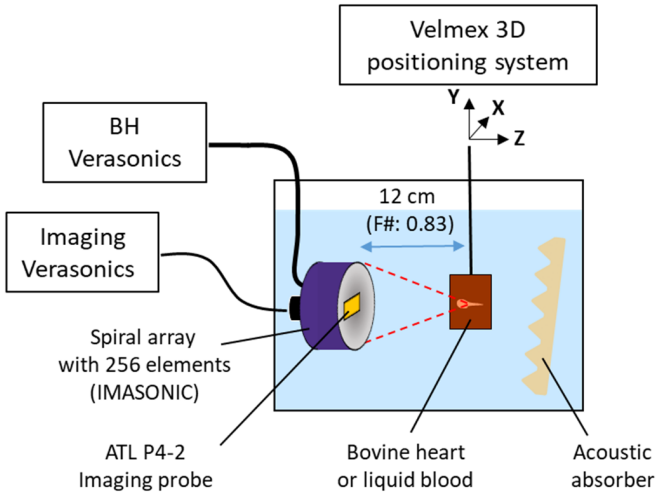


Fig. 1. Schema of the experimental setup for BH exposures of liquid blood or ex vivo tissue samples and data acquisition for coaxial B-mode and Doppler imaging. 256-element HIFU array and ATL P4-2 imaging probe were connected to separate V-1 Verasonics systems to control therapeutic and imaging pulses, respectively.

and degree of liquefaction. Thus, obtained observations of lesion progression were correlated with Doppler-measured velocity maps within the lesion following each BH pulse, and candidate metrics were proposed for the determination of treatment completeness.

## II. Methods

### A. Experimental Setup

The experimental setup used in this study is illustrated in Fig. 1. A 1.5 MHz 256-element spiral array with electronic focus steering custom-designed for volumetric BH treatments of abdominal organs (IMASONIC, Voray-sur-l'Ognon, France) was driven by a power enhanced Verasonics V-1 acquisition platform (Verasonics Inc., Kirkland, WA, USA) [28]. The transducer has a 14.4 cm aperture and 12 cm radius of curvature (f-number of 0.83), and circular central opening of 4 cm diameter to accommodate an ultrasound imaging probe. A typical BH pulsing protocol was used: 10 ms pulses were delivered at PRF of 1 Hz [29]. A 64-element phased array with a 2 cm aperture (ATL P4-2, Phillps, Bothell, WA, USA) coaxially mounted at the central opening of the HIFU array was controlled by a separate Verasonics V-1 system for B-mode and BCD imaging. The HIFU and imaging transducer assembly was placed into a tank filled with de-ionized and degassed water at room temperature, with dissolved oxygen less than 10% of the saturation level.

Fresh bovine myocardium tissue and blood were acquired from a local abattoir and treated within 48 h. The blood was immediately mixed in a plastic container with the anticoagulant solution (CPD, C7165; Millipore-Sigma, St. Louis, MO, USA) at 9:1 volume ratio. The myocardium tissue samples were trimmed, degassed in saline in a desiccant chamber for 1 h, and embedded into degassed agarose gel to be fit in a 4 × 4 × 8 cm size holder on the day they were obtained. The prepared tissues and blood were kept on ice in the refrigerator. Then immediately before the experiment, the blood was degassed for 1 h and poured into a latex balloon with approximately 8 cm diameter when expanded, sealed, and fixed in the holder. All tissues were kept at room temperature for approximately 1 h before the experiment. The sample holders were attached to a 3-D positioning system (Velmex Inc., Bloomfield, NY, USA) and placed into the water tank in front of the transducer focused inside the sample. A rubber acoustic absorber was placed behind the sample to reduce the reverberation artifact on US imaging.

### B. HIFU Focal Pressure Levels and Focus Position

The HIFU focus position was preregistered with the imaging system as described below. At the shock-forming output level of the transducer, the maximum peak positive pressure position was found in water using a fiber-optic probe hydrophone (FOPH 2000, RP Acoustics, Leutenbach, Germany). The tip of FOPH in the corresponding B-mode image thus corresponded to the HIFU focus in water. To account for an axial shift of the focus position due to the difference in the sound speed in water and in the tissue causing refraction at the water/tissue interface, additional adjustment of the axial focus position was performed before each experiment. The average values for the speed of sound in water and tissue were taken from the literature (see Table I), and Snell's law was used to estimate this additional shift (which ranged within 1–3 mm). The resulting HIFU focus position was displayed on the B-mode images as a pink cross.

The in situ peak positive ($p^+$), negative ($p^-$) pressures, and shock amplitude ($p_s$) at the HIFU focus in ex vivo tissue samples were obtained from numerical simulations of the nonlinear field using the Westervelt equation, performed for experimental conditions of our study. The simulation method and its validation by hydrophone measurements in water for this HIFU array is described in detail in previous studies [28], [30]. The acoustic properties of the samples used in the simulation are specified in Table I [29], [31]. The focal pressure levels noted throughout this article were obtained from these simulations.

### C. Ultrasound Imaging Sequence

The ultrasound imaging sequence used in this work is illustrated in Fig. 2. Each BH pulse was immediately followed by a plane-wave Doppler ensemble and then a B-mode sequence. B-mode was conventional 48 ray-line imaging with 3 MHz center frequency and 4.5 kHz PRF. The beamforming and scan conversion processing of the B-mode was performed by Verasonics.

The plane-wave Doppler ensemble consisted of 90 pulses of three cycles with 2.81 MHz center frequency, 1.3 MPa pressure amplitude measured with needle hydrophone (HNR-0500, ONDA Corporation, Sunnyvale, CA, USA) in water at the HIFU focus, and the beamwidth of 1.6 cm/0.45 cm at −6 dB level transverse/elevational, respectively. Kaiser amplitude window was used to suppress the side lobes both when transmitting and receiving the Doppler pulses.

TABLE I
PHYSICAL PROPERTIES OF BOVINE BLOOD AND MYOCARDIUM TISSUE

| | Density, kg/m$^3$ | Sound speed, m/s | Attenuation, Np/cm (at 1.5 MHz) | Nonlinear parameter | Volumetric heat capacity, J/C/m$^3$ | Dynamic viscosity, Pa·s | Shear wave speed, m/s |
|---|---|---|---|---|---|---|---|
| Bovine blood | 1,060 | 1,580 | 0.036 | 4 | $3.834\times10^6$ | $3.65\times10^{-3}$ | N/A |
| Bovine myocardium | 1,060 | 1,570 | 0.09 | 4 | $3.940\times10^6$ | N/A | 5 |

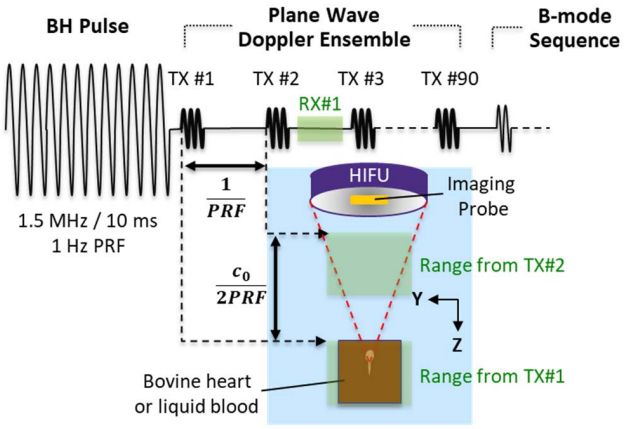


Fig. 2. Schema of the ultrasound imaging sequence. 90-pulse plane wave Doppler ensemble was emitted immediately after the BH pulse, and then 48-ray-line B-mode sequence followed. Echoes from two consecutive Doppler transmit pulses (for example, TX1 and TX2) were received within a single receive gate. Echoes of TX1 covered the ROI, while echoes of TX2 arriving at the same time corresponded to the area of water-filled standoff with minimal scattering, and thus, did not contaminate the signal.

Based on the round-trip time-of-flight in water, calculated as

$$\mathrm{PRF}_{\max} = \frac{c_0}{2d} \tag{1}$$

where $c_0$ is the sound speed and $d$ is the distance from the probe to the furthest part of the region of interest (ROI), the maximum available Doppler PRF, $\mathrm{PRF}_{\max}$, for $d = 18$ cm is 4.2 kHz. With this PRF, the maximum measurable speed calculated as

$$|v|_{\max} = \frac{\mathrm{PRF}_{\max} \cdot c_0}{4 f_0} \tag{2}$$

where $f_0$ is the center frequency of the Doppler pulse is 52 cm/s [32]. The presence of velocities exceeding this value would cause an aliasing artifact on the BCD image. According to our preliminary studies, velocities of bubbles and debris inside the lesion immediately after a BH pulse could reach several meters per second, and thus, higher PRF was needed to avoid aliasing.

To address this challenge, high PRF plane-wave Doppler was used, as illustrated in Fig. 2. Twofold increase of the PRF was achieved based on the fact that at least half of the propagation distance from the imaging transducer to the ROI was occupied by water with minimal scattering. Unlike conventional Doppler imaging, in high PRF Doppler, the imaging probe transmits two pulses within the round-trip time of the flight window, for example, TX1 and TX2 (see Fig. 2). Although echoes from the two pulses are recorded within one receive gate, the gate can be positioned in such a manner that echoes from the first pulse would cover the ROI, whereas echoes from the second pulse could only arrive from the water-filled standoff with no scattering. With this technique, PRF and the corresponding maximum measurable speed can be increased twofold and reach 9.375 kHz and 128 cm/s, respectively. At this PRF, the 90-pulse Doppler ensemble was 9.6 ms long.

### D. BCD Signal Processing

Scan-converted in-phase and quadrature (I/Q) data was saved onto the internal hard drive by Verasonics and then post-processed to obtain BCD images. The I/Q data were converted into BCD images within a sliding processing window that included 12 Doppler ensemble pulses and was shifted along the 90-pulse ensemble with a step size of 1 pulse to obtain each BCD image for a total of 79 BCD images. Conventional color Doppler processing in MATLAB was used for each of the 12-pulse processing windows as follows. The slow-time data were wall-filtered with a second-order infinite impulse response (IIR) high-pass filter with an 80 Hz cut-off frequency. Because only 12 pulses were included in the processing window, the projection initialization technique was implemented to improve the high-pass filter performance [33]. Doppler power and velocity were then calculated by Kasai et al. [34] using an autocorrelation algorithm with one sample lag $R(1)$. Doppler power, defined as the absolute value of $R(1)$, and mean Doppler frequency shift ($\bar{\omega}$) defined as the product of Doppler PRF and phase of $R(1)$ were calculated. The axial component of the velocity $\bar{v}$ was then obtained as directly related to $\bar{\omega}$

$$\bar{v} \cdot \cos\theta = \frac{\bar{\omega} c_0}{4\pi f_0} \tag{3}$$

where $\theta$ is the angle between the direction of motion and the Doppler pulse propagation direction. Because it was expected that the motion of the bubble remnants and tissue debris would be induced by acoustic radiation force, which is primarily directed axially, the dominant component of the velocity was also expected to be axial. This expectation was validated qualitatively by observing the real-time B-mode image during the anticoagulated blood experiment described in the following paragraph (Supplement videos 1 and 2). Thus, hereinafter the axial velocity $\bar{v} \cdot \cos\theta$ will be referred to as the velocity. Next, the BCD image pixel's Doppler power falling below the power threshold was identified and assigned

a zero value. The power threshold was selected as the larger value of the double average of the Doppler power level and the power level corresponding to the maximum background noise. To display the resulting velocity maps, a traditional color Doppler colormap was used: motion directed toward the imaging probe was assigned a positive sign and warm color range (red to yellow), and motion directed away from the transducer—the negative sign and cold color range (blue to cyan). For display, the BCD images were overlaid onto the corresponding B-mode image.

### E. BH Exposures of Anticoagulated Blood

Anticoagulated blood served as a model for a limiting case of very large, fully liquefied BH lesions. The HIFU array focus was positioned inside the 8-cm diameter blood-filled balloon at a distance of 2 cm from its proximal surface. BH pulses were delivered to this single focus location at different BH output levels. The in situ $p^+$ and $p^-$ within each pulse were 4.3–124.2 and −3.5 to −17.1 MPa, respectively, based on the simulation as described in Section II-B. BCD data were acquired five times per BH output level. Each acquisition was separated by at least 5 s to allow enough time for the movement from the previous BH pulse to stop. In order to increase Doppler signal-to-noise ratio (SNR) for lower BH levels and correspondingly lower flow velocities, a larger Doppler processing window was used. Instead of using 12 pulses as with the higher range (in situ $p^+ = 101.9$–$124.2$ MPa), 40 and 85 pulses were applied for $p^+ = 17.5$–$87.8$ MPa and $p^+ = 4.3$–$14.1$ MPa, respectively. This increased overall ensemble length from 1.3 to 4.3 and 9.1 ms, respectively, and the associated averaging of the velocity measurement over that time period was not expected to affect the measurement precision substantially. To measure the higher velocities in excess of 200 cm/s for in situ $p^+$ at the range of 101.9–124.2 MPa, $\bar{\omega}$ was compensated to range within $-2\pi$ to 0 instead of $-\pi$ to $\pi$, so that the measurable velocity range was −240 to 0 cm/s. This approach is only possible when the velocity detected at every spatial point is expected to have the same direction as it was in a liquid. For each exposure, the absolute value of the maximum velocity within the ROI, $v_{\max}$ was extracted from the BCD image obtained within the first Doppler processing window.

### F. Single Focus BH Exposures of Soft Tissue

Bovine myocardium tissue motion immediately following a BH pulse was investigated as the opposite limiting case using color Doppler measurements and theoretical estimations. To avoid tissue liquefaction but still have sufficient Doppler SNR for velocity estimation, a BH pulse was delivered at the output level just below the boiling threshold. With this BH power, $p^+$, $p^-$, and shock amplitude ($p_s$) were 95.5, −15.2, and 76.4 MPa, respectively. The HIFU focus was positioned at a depth of 1.8 cm in tissue. A single BH pulse was delivered to the tissue, and the same procedure was repeated 11 times to the other locations in the tissue. In terms of the Doppler processing, an IIR low pass filter was used instead of a high-pass filter because tissue motion was expected to be relatively slow. As a metric, $v_{\max}$ was investigated as a function of time after BH pulse.

The theoretical tissue velocity at the focus was calculated by considering radiation force from a nonlinear BH pulse with shock fronts on the tissue [35], [36], as

$$v_z(t) = \frac{\beta a f p_s^3}{6\rho^3 c_t c_l^5} V(T) \tag{4}$$

where $\beta$ is the nonlinear parameter of tissue, $a$ is the HIFU beam radius, $f$ is the BH source frequency, $p_s$ is the shock amplitude, $\rho$ is tissue density, $c_t$ is shear wave speed, $c_l$ is longitudinal wave speed in tissue, and

$$V(T) = \begin{cases} 0, & (T < 0) \\ \dfrac{T}{1+T^2}, & (0 < T < T_0) \\ \dfrac{T}{1+T^2} - \dfrac{T-T_0}{1+(T-T_0)^2}, & (T > T_0) \end{cases} \tag{5}$$

where $T = (c_t t/a)$, $T_0 = (c_t t_0/a)$, and $t_0$ is the BH pulse duration. According to (5), during the BH pulse, the velocity initially increases with time in the direction of ultrasound propagation, then decreases with $(1/T)$ asymptotic behavior. Immediately after the end of the BH pulse, the velocity in the opposite direction rapidly increases and then decays, representing the first tissue rebound. The physical properties used in this estimation are listed in Table I.

### G. Volumetric BH Treatments in Ex Vivo Bovine Myocardium

Two types of volumetric BH treatments with electronic focus steering were performed in bovine myocardium samples and are illustrated in Fig. 3. The first type, resulting in an elemental-volume treatment, corresponded to a 2-D distribution of the discrete focus steering positions shown in Fig. 3(a). The distribution consisted of 65 target points in the $XY$ plane (i.e., elevational plane of the imaging probe) orthogonal to the HIFU axis, and the central target point corresponded to the HIFU focus. The target locations were positioned in a 13 × 5 rectangular grid with 0.1 cm spacing: $-0.6 \le x \le 0.6$ cm and $-0.2 \le y \le 0.2$ cm. The steering limits of the BH beam in the elevational direction of the imaging probe were selected to be within the elevational beamwidth of the probe at the HIFU focus (4.5 mm). These limits allowed for expanding the ablation volume achievable with only electronic steering of the BH pulse.It was, however, less sensitive to observe motion away from the imaging planes. Based on the hydrophone measurements, the pressure amplitude of the imaging pulse diminished to 88% and 57% one and two millimeters off the imaging plane. Nevertheless, this reduction in sensitivity still remained sufficient to image bubble motion. To achieve the same in situ pressure amplitude at all target locations via electronic steering, power compensation specific to each location per characterization reported previously [28] was applied. In this case, $p^+$, $p^-$, and $p_s$ were 117.7, −16.6, and 108.2 MPa, respectively. The power compensation was achieved by controlling the apodization factor on all elements rather than the system driving voltage, as it provided faster

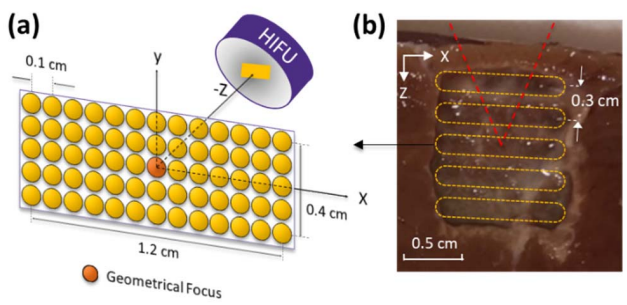


Fig. 3. (a) Target locations marked as yellow circles: 65 target points spaced 0.1 mm apart in the $-0.6 \leq x \leq 0.6$ cm, $-0.2 \leq y \leq 0.2$ cm range within an elemental treatment volume. (b) Five elemental treatment volumes with 0.3 cm spacing (yellow dashed contours) on the actual photograph of the composite-volume BH lesion bisected through the imaging plane *xz*. Target locations (a) were located in the middle of each contoured area along the *z* coordinate.

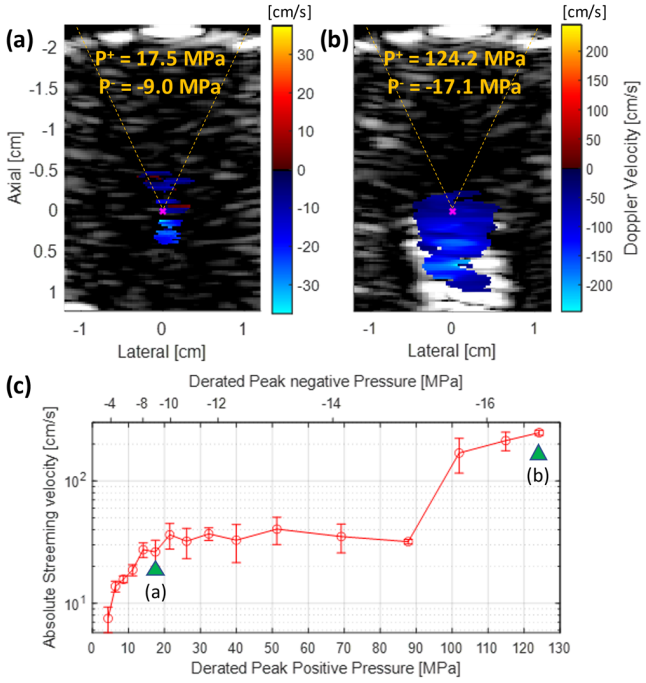


Fig. 4. Blood streaming visualization by color Doppler for (a) low BH power (in situ focal pressures indicated in yellow) and (b) high BH power. The HIFU focus is denoted by the pink 'x' mark. (c) Measured absolute value of maximum streaming velocity in the liquid blood. Shock amplitude of 80.6 MPa is formed at 101.9/15.6 p+/p− peak focal pressures.

switching between target locations and facilitated higher PRF of the BH treatment [28], [37]. A single BH pulse was applied to all 65 targets in the rectangular grid in a sequence, and the sequence was repeated until each location received 15 pulses. In each sequence, the central line within the imaging plane ($y = 0$) was treated first, followed by the lines just outside of the imaging plane within the elevational plane: $y = -0.1$, 0.1, $-0.2$, and 0.2 cm. The order of the sonication points within a line was random.

The second type—composite-volume treatment—was achieved by merging five elemental-volume treatments along the HIFU axis $z$ with 0.3 cm spacing [see Fig. 3(b)]. One elemental volume corresponded to the position of the geometrical focus of the HIFU array, $z = 0$, two volumes were positioned postfocally ($z = 0.3$ and 0.6 cm), and the other two prefocally ($z = -0.3$ and $-0.6$ cm). To eliminate the shielding effect of the residual bubbles from the already treated area, the volumes were treated consecutively, moving from the furthest postfocal volume to the one most prefocal.

## III. Results

### A. BH-Induced High-Velocity Streaming in Anticoagulated Blood

Two representative color Doppler images for lower ($p^+ = 17.5$ MPa, $p^- = -9.0$ MPa in situ) and higher ($p^+ = 124.2$ MPa, $p^- = -17.1$ MPa in situ) BH output levels are shown in Fig. 4(a) and (b), respectively. The boundary of the latex balloon containing the blood is seen as a bright white interface in the background B-mode image at $-2$ cm axial location. While the observed velocity ranges are very different for these two cases, the direction of motion is away from the HIFU transducer, as expected. At the lower output level, the maximum observed velocity of 35 cm/s was reached on the HIFU axis slightly postfocally (around 0.2 cm), whereas at the higher output level, the maximum velocity was almost an order of magnitude higher (over 200 cm/s) and was reached about 0.6 cm postfocally. Theoretically, the maximum velocity would be expected at the focus, where the acoustic radiation force is the largest. The observed postfocal shifts of the maximum may correspond to the fast-moving liquid displacement from the focus over the duration of the Doppler processing window. The area of detectable motion was also noticeably larger in both dimensions in the higher output case. In addition, a large hyperechoic area can be seen at the focus on the B-mode image in Fig. 4(b), clearly indicating the formation of bubbles at that output level, which could enhance radiation force and streaming.

The value of the maximum velocity, $v_{\max}$, determined from the color Doppler images immediately following the BH pulse and averaged over five different exposures, is plotted in Fig. 4(c) for different output levels corresponding to the in situ $p^+$ (bottom abscissa) and $p^-$ (upper abscissa); error bars correspond to standard deviation. The measured maximum velocity values gradually increase, as expected, below $p^+ = 20$ MPa and $v_{\max} = 30$ cm/s, then plateau at 30–40 cm/s within the range of $p^+$ from 20 to 90 MPa. This may be attributed to the fact that the turbulent effect begins at this velocity range. The velocity of 40 cm/s, at which the discrepancy becomes prominent, corresponds to the Reynolds number of 1500, which is a little lower than what is generally considered as nonlaminar flow (Re = 2000). Further, blood is known to be a non-Newtonian fluid, with viscosity decreasing by orders of magnitude at high shear rates [38]. This can result in an exponential increase in Reynolds number and a significant turbulent effect as the streaming velocity increases. Interestingly, at 90–100 MPa, there was a discontinuity: the velocity increased abruptly to about 200 cm/s and continued to grow with $p^+$. There are two potential reasons for this

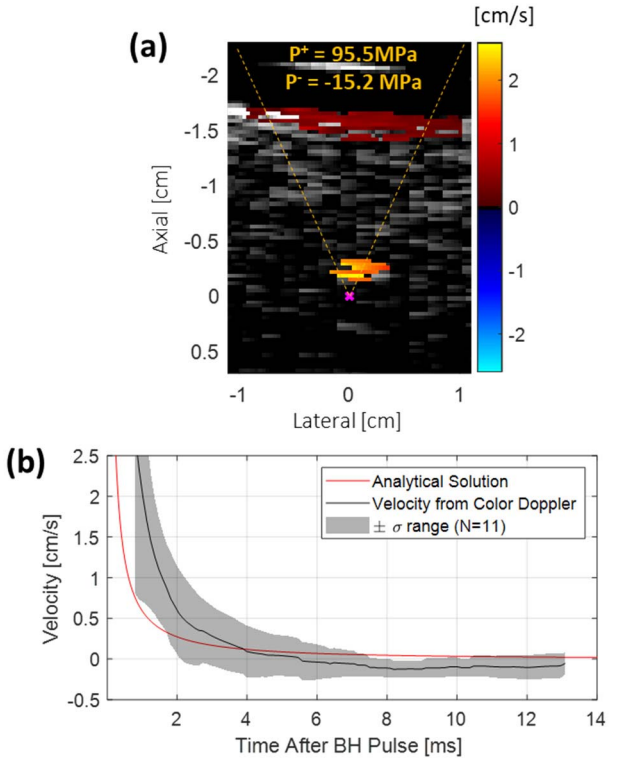


Fig. 5. (a) Color Doppler image for the first Doppler processing window in myocardium tissue for pulsed exposures in the absence of boiling and liquefaction. (b) Tissue motion from the color Doppler compared to the analytical solution (4) and (5). The mean value from 11 different Doppler acquisitions is represented by black line and its standard deviation is shown as the transparent gray zone.

observation; first, this output level corresponds to the shock formation in HIFU focal waveform [28], and thus, substantially increased acoustic radiation force [36]. In addition, a hyperechoic region corresponding to bubble activity was also first observed on B-mode images at that level, which would further enhance acoustic radiation force.

### B. BH-Induced Motion in Intact Soft Tissue

The limiting case opposite to that of the fully liquid medium considered above is the case of intact soft tissue in the absence of liquefaction. A representative example of a color Doppler image corresponding to the first 12 pulses in the Doppler ensemble is shown in Fig. 5(a). Unlike the case of liquid blood, the tissue moved toward the transducer at a low but detectable velocity of a few cm/s. This motion represents the rebound of elastic tissue following the termination of acoustic radiation force applied by the BH pulse. Note that the surface of the sample is also moving in the same direction, albeit at a much lower velocity, although it is located outside of the focal area. Most probably, this is due to the partial reflection of the BH pulse from the water-sample interface, and therefore, enhanced radiation force. Fig. 5(b) compares the evolution of the measured and theoretically estimated velocity over time after the BH pulse. The mean and standard deviation from eleven different acquisitions are represented by a black line and gray shade, respectively. The velocity values are in good

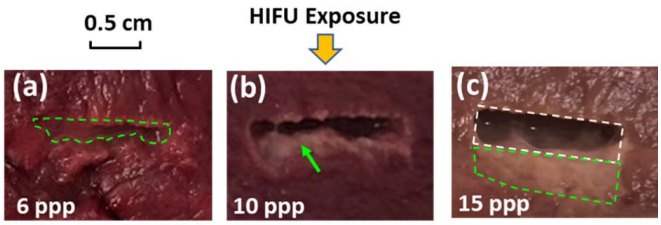


Fig. 6. Photographs of the elemental-volume BH treatments bisected in the imaging plane after specified number of BH pulses per target point (ppp). (a) 6 ppp, (b) 10 ppp, and (c) 15 ppp. BH pulse was incident from the top of the images. Green dashed boxes [in (a) and (c)] and arrow [in (b)] indicates partial liquefaction area and white boxes in (c) indicates fully liquefaction area.

agreement, and both graphs decline exponentially over time. Of note, the measured tissue motion changed direction within a 4–6 ms time frame, representing the second rebound. This second rebound was not observed in the theoretical curve because the theoretical model assumes uniform radiation force in the axial direction.

### C. Elemental-Volume BH Treatment in Bovine Myocardium Tissue

Fig. 6(a)–(c) shows representative photographs of the elemental volumetric BH lesions bisected along the ultrasound imaging plane after 6, 10, and 15 BH pulses were delivered per target point, respectively. All photographs were taken after rinsing out the liquefied debris from the cavity. BH sonications were incident from the top of the images in Fig. 6. Partial tissue liquefaction can be observed in Fig. 6(a) within the lesion marked by the green dashed line. The proximal border is relatively smooth, but the distal border is irregular. On the other hand, the lesion Fig. 6(b) and (c) show more uniform liquefaction with sharp and smooth proximal and side boundaries and slightly irregular distal boundaries. For example, an area of residual connective tissue can be observed at the distal border on the left side of the cavity in Fig. 6(b), marked as a green arrow. Notably, the lateral size of all three lesions is the same (1.3–1.5 cm) and corresponds to the size of the planned BH treatment grid. The axial size, however, increases with the number of pulses and is about 0.2, 0.4, and 0.7 cm after 6, 10, and 15 pulses, respectively. The degree of tissue fractionation also increases with the number of pulses. The complete lesion in Fig. 6(c) has a fully liquefied area of 0.4 cm axial size and is indicated as white dashed box and also has a wider blanched border of 0.2–0.3 cm width at the distal border marked as green dashed box, which was observed previously in BH treatments of bovine myocardium [39]. The border most probably represented partially fractionated tissue resulting from the incomplete merging of the distal "tails" of the BH lesions.

Fig. 7 shows the BCD images and corresponding metrics from a representative elemental-volume treatment. The top, middle, and bottom figures correspond to the target locations at the center ($x = 0$, $y = 0$), furthest elevational margin ($x = 0$, $y = 0.2$ cm), and furthest lateral margin ($x = -0.6$ cm, $y = 0$), respectively [target (a), (b), and (c)]. BCD images

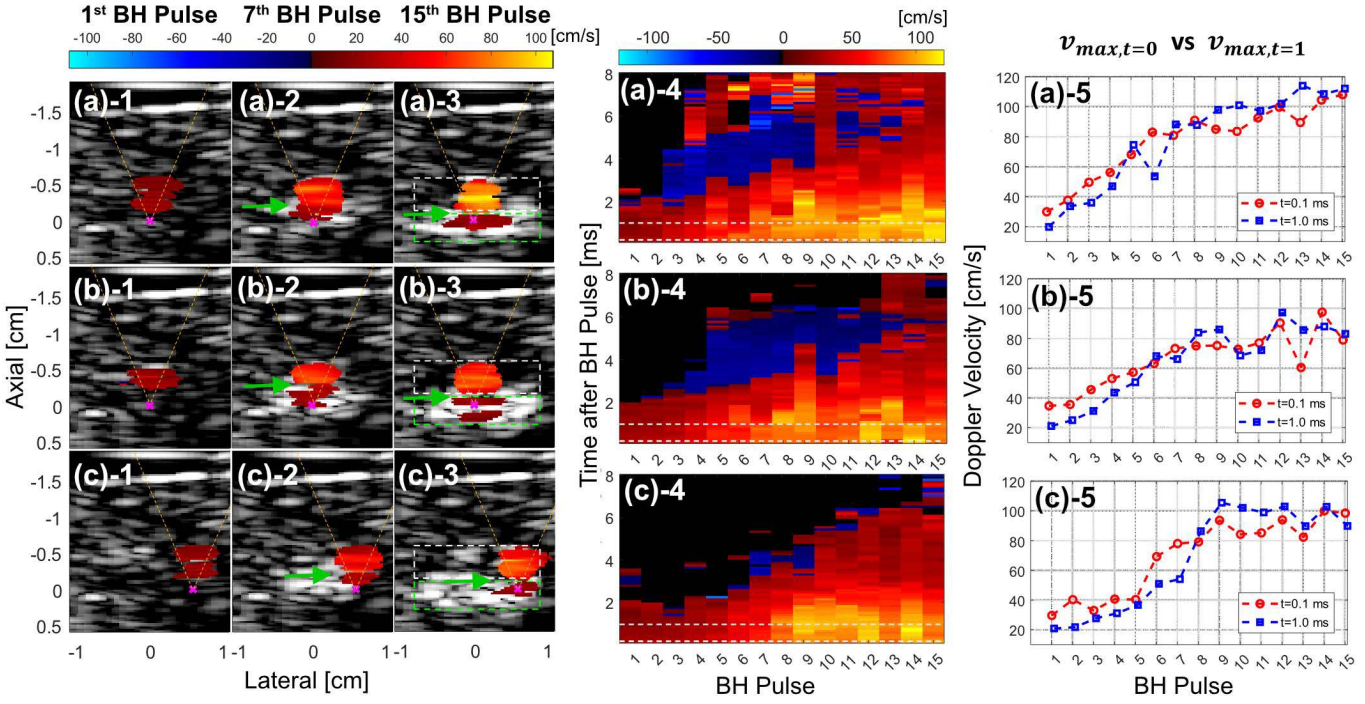


Fig. 7. BCD images and metrics for elemental-volume BH treatment for three HIFU focus positions. (a) center ($x = 0$, $y = 0$), (b) furthest elevational margin ($x = 0$, $y = 0.2$ cm), and (c) furthest lateral margin ($x = -0.6$ cm, $y = 0$). The first three columns show BCD images for the 1st, 7th, and 15th BH pulses, the fourth column shows the maximum velocity determined from BCD with respect to the BH pulse number and time after BH pulse, and the fifth column shows maximum velocity dependence on the BH pulse number at two specific time points after the BH pulse corresponding to the white dashed lines in the fourth column: immediately (red dashed line), and 1 ms after BH pulse (blue dashed line).

in the left three columns in Fig. 7 are superimposed on the corresponding B-mode for the 1st, 7th, and 15th BH pulses at the time point immediately after the BH pulse. As seen, the motion is directed toward the transducer regardless of the target location and the number of BH pulses delivered. This behavior is similar to the intact tissue motion mentioned above, but the velocity is about tenfold higher, around 20–30 cm/s for the first BH pulse. The area of detectable motion in all target points after the first BH pulse is located 0.1–0.2 mm prefocally and is 0.28–0.49 cm axially. The axial size of that area is extended to 0.53–0.59 and 0.70–0.79 cm for the 7th and 15th BH pulses, respectively. This size for the 15th BH pulse corresponds well with the axial size of the BH lesion in Fig. 6(c). The Doppler velocity is uniform for the first BH pulse; on the other hand, there is noticeable velocity variation axially as marked by a green arrow for the 7th and 15th BH pulses: the velocities immediately above and below the arrow are 55 and 30 cm/s for the 7th BH pulse [see Fig. 7(a)-2] and 71 and 22 cm/s for the 15th BH pulse [see Fig. 7(a)-3].

Also, the axial size of the area above the arrow is about 0.35 and 0.45 cm for the 7th and 15th BH pulses, respectively. The white and green boxes for the 15th BH pulse indicate large and small velocity areas, respectively, and correspond well with the fully and partially liquefied area mentioned in Fig. 6(c). For the different target locations, the overall size of the areas is similar, but the axial size in Fig. 7(b)-1 and the size above the arrow in Fig. 7(b)-2 are slightly smaller, which

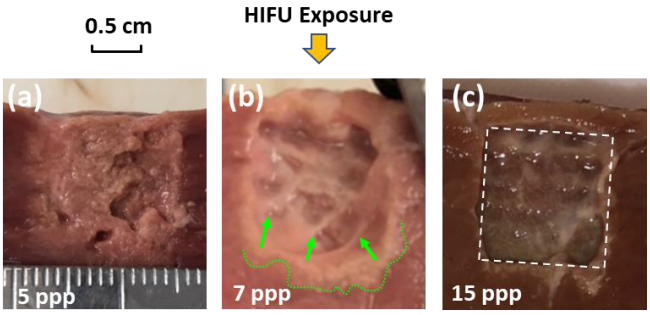


Fig. 8. Photographs of composite-volume treatments bisected in the imaging plane after specified number of BH ppp. (a) 5 ppp, (b) 7 ppp, and (c) 15 ppp. The BH exposure of all lesions was directed from the top to the bottom of the images. White box in (c) indicates the targeted area.

may result from the fact that the imaging plane is slightly outside.

Three figures in the fourth column [Fig. 7(a)-4, (b)-4, and (c)-4] show the maximum velocity value in the BCD images, $v_{\max}$, with respect to the number of BH pulses and time after each BH pulse. As seen, for the first and second BH pulses, regardless of the target location, the rebound tissue motion settles down in approximately 2 ms, and no motion is detected after that. As the treatment progresses, i.e., within the range of the 3rd–13th BH pulse, the second rebound motion displayed in

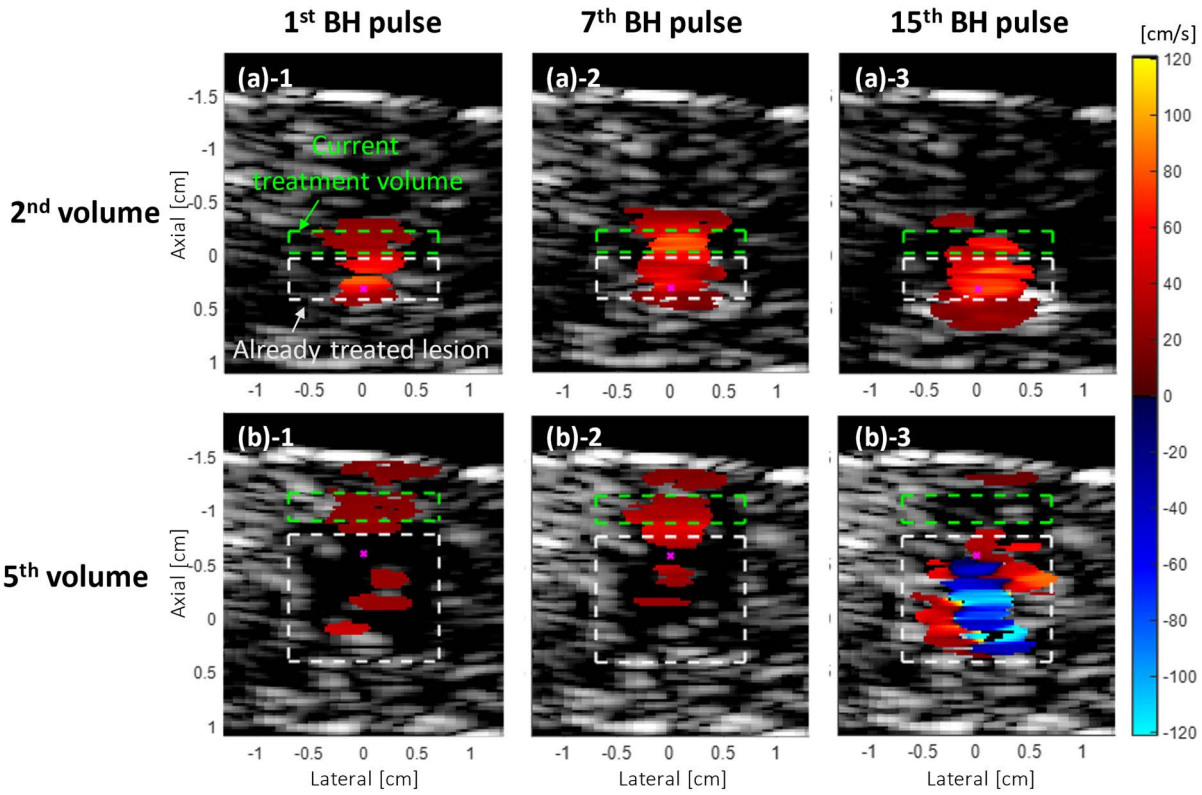


Fig. 9. BCD images at 1 ms after BH pulse delivered to the central target point ($x = 0$, $y = 0$) for (a) the 2nd and (b) 5th elemental treatment volumes that form a composite-volume BH treatment. Current elemental-volume treatment and previously treated volume are marked as green and white dashed boxes, respectively. The 1st BH pulse (first column), 7th BH pulse (second column), and 15th BH pulse (third column) were selected for the display.

blue is observed, and its onset is gradually delayed from 2 to 5 ms. The second rebound is observed more clearly in Fig. 7(a) and (b) compared to Fig. 7(c), which may be attributed to the fact that Doppler SNR for this laterally steered target was too low to detect all motion over the entire time range so that the rebound motion for which Doppler power is lower than the threshold was filtered out.

In the rightmost (fifth) column graphs, the maximum velocity values $v_{\max}$ immediately after ($v_{\max,t=0}$) and 1 ms after BH pulse ($v_{\max,t=1}$) as functions of the BH pulse number are shown. The overall trends of $v_{\max,t=0}$ and $v_{\max,t=1}$ are very similar between the three focus positions Fig. 7(a)–(c): both metrics gradually increase from 20–30 to 90–100 cm/s over the first nine BH pulses and then plateau. This saturation corresponds to the formation of adjacent fractionated lesion that 9–10 BH pulses can generate, as shown in Fig. 6(b). However, note that the initial value of $v_{\max,t=1}$ is lower compared to $v_{\max,t=0}$, whereas the saturation value is similar Therefore, $v_{\max,t=1}$ appears to be a more sensitive candidate metric of the liquefaction progression. Specifically, the rate of change (ROC) between the maximum and minimum values for the $v_{\max,t=0}$ and $v_{\max,t=1}$ of target (a) is 262% and 475%, respectively, calculated as

$$\mathrm{ROC}(\%) = \frac{\max(v_{\max}, t = t_0) - \min(v_{\max,t=t_0})}{\min(v_{\max,t=t_0})} \times 100 \quad (6)$$

where $t_0$ is 0 or 1 depending on the metric.

### D. Composite-Volume BH Treatment in Bovine Myocardium Tissue

Photographs in Fig. 8(a)–(c) show representative cross sections of the composite-volume lesions obtained by merging five elemental-volume lesions with a different BH pulse number: 5, 7, and 15 pulses per target, respectively. With five pulses per target [see Fig. 8(a)], noticeable residual tissues are observed throughout the lesion, and the lesion boundary from intact tissue is unclear. With seven pulses per target [see Fig. 8(b)], the lesion volume is more homogenously liquefied, with occasional strands of residual tissue attached to the surrounding intact tissue (green arrows) and a somewhat irregular boundary (green dashed line). A further increase to 15 pulses per target [see Fig. 8(c)] resulted in a homogenously liquefied volume with smooth and sharp boundaries.

Shown in Fig. 9 are BCD images corresponding to the 1st, 7th, and 15th BH pulses delivered to the central target point ($x = 0$, $y = 0$) at $t = 1$ ms after sonicating the second and fifth elemental-treatment volumes. Since the lesion was formed in order from postfocal to prefocal elemental volumes, the size of the preexisting lesion differed between the second and fifth treatment volumes, as indicated by the white dashed box. A green dashed box outlines the current treatment volume with an axial position corresponding to the boiling bubble shown on the B-mode for the first BH pulse of each treatment volume. Unlike a single elemental-volume

treatment, the BCD observations here differ depending on the size of the adjacent previously treated tissue. In the case of generating the second elemental volume, motion is observed in the preexisting first elemental-volume lesion, as well as in the current treatment volume. The motion in both volumes is directed toward the transducer, but the velocities in the two volumes are quite different. The velocity inside the current volume is initially lower than in the preexisting one, then becomes higher for the 5th–9th BH pulses and lower again after the tenth pulse. The distal boundary of the lesion starts to be extended after the seventh BH pulse, similar to the elemental-volume treatment. This fact also corresponds to the irregular distal boundary, as shown in Fig. 8(b).

In the fifth treatment volume, with a large preexisting liquid volume composed of four elemental volumes, several separate areas of motion toward the transducer are observed in both the current and preexisting volumes during the first part of the treatment, i.e., pulses 1st–8th. Compared to the second treatment volume case, the trend of maximum velocity location for the 1st–8th pulses was similar; however, for the 15th BH pulse, a diminished motion was detected in both the region distally to the preexisting lesion and the current treatment volume. As the two volumes start to merge after the eighth BH pulse, the observed motion changes direction, i.e., streaming in direction of the wave propagation is observed at gradually increasing velocity as treatment progresses. Ultimately, as indicated in Fig. 9(b)-3, the streaming velocity reaches 120 cm/s, and streaming in the opposite direction develops on both sides of the focus, consistent with expectations for streaming in confined volume. This spatial pattern of velocity was only observed for the fourth and fifth elemental treatment volumes, i.e., only for a large liquefied volume with an axial size exceeding 1 cm.

Based on the above observations, additional metrics were investigated for the composite-volume treatment at $t = 1$ ms after BH pulse: the distance between the BH target location and maximum velocity location ($\vec{\Delta}x_{\max,t=1}$) and velocity at the target position ($v_{\text{targ},t=1}$). These two metrics are determined for the current target location within a certain axial range that corresponds to the span of the current treatment volume (i.e., axial size of the green dashed box in Fig. 9). The distance $\vec{\Delta}x_{\max,t=1}$ is a 2-D scalar defined as the lateral and axial distances between the location of $v_{\max,t=1}$ and center point of the axial range within the ultrasound imaging plane. The values of $\vec{\Delta}x_{\max,t=1}$ averaged over all targets within the same elemental treatment volumes for the BH exposure described in Fig. 9 are plotted against the BH pulse number in Fig. 10. Reflecting the observations from the BCD images above, the axial component of $\vec{\Delta}x_{\max,t=1}$ for the 2nd–5th treatment volumes is positive, i.e., is distal relative to the center of the treatment volume. For those volumes, the metric is initially 0.2–0.6 cm, then it decreases to approximately 0.1 cm at the 4th–5th BH pulse regardless of the treatment volume number, and then progressively increases and saturates depending on the treatment volume location. Interestingly, the saturation level for the 2nd and 3rd treatment volumes was nearly identical to the value corresponding to the initial BH pulse and was higher for 4th and 5th treatment volumes. Unlike the axial component of $\vec{\Delta}x_{\max,t=1}$, its lateral component remained almost constant at 0.1 cm over all treatment points of all treatment volumes.

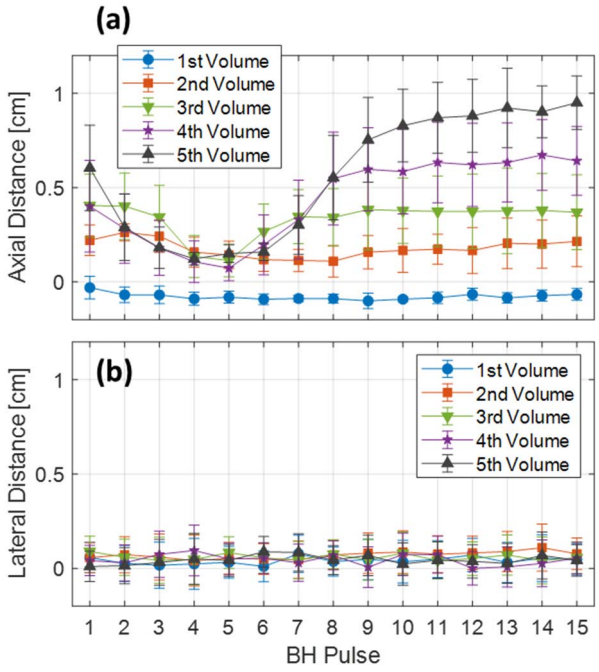


Fig. 10. (a) Axial and (b) lateral distance between the target point and maximum velocity location for each of consecutive elemental treatment volumes averaged over all targets within the same elemental treatment volume. Error bars correspond to the standard deviation.

Based on the observations of BCD during composite-volume BH treatment described above, it is clear that $v_{\max}$ alone is not a reliable indicator of the degree of tissue liquefaction in the current treatment volume because of the interaction with the preexisting distal volumes. At the same time, the lateral component of the maximum velocity location $\vec{\Delta}x_{\max,t=1}$ is stable over the treatment and is within 1 mm. For these reasons, the maximum velocity at $t = 1$ ms after BH pulse within the current treatment volume, $v_{\text{targ},t=1}$, was selected as a metric and termed "target velocity."

Fig. 11(a) shows the $v_{\text{targ},t=1}$ map for the selected BH pulses superimposed on the photograph of the cross sections of a lesion shown in Fig. 8(c). Each arrow in Fig. 11(a) represents $v_{\text{targ},t=1}$ averaged over targets along the elevational direction and positioned at the corresponding target location. As seen, the value of $v_{\text{targ},t=1}$ is initially low and uniform across all target points, then gradually increases while maintaining its uniformity until around the 5th–6th BH pulse; however, from the seventh BH pulse, the trends change depending on the treatment volume. For the first and second volumes (bottom two rows of arrows), the velocity continues to increase and slowly saturates. For the other three volumes it either does not change or decrease. For all elemental treatment volumes, the pattern of the $v_{\text{targ},t=1}$ map does not change noticeably within the 10th–15th BH pulses. The graph in Fig. 11(b) shows $v_{\text{targ},t=1}$ averaged in all targets within the same treatment volume versus the number of BH pulses. As expected, the line for the first treatment volume exhibits similar results

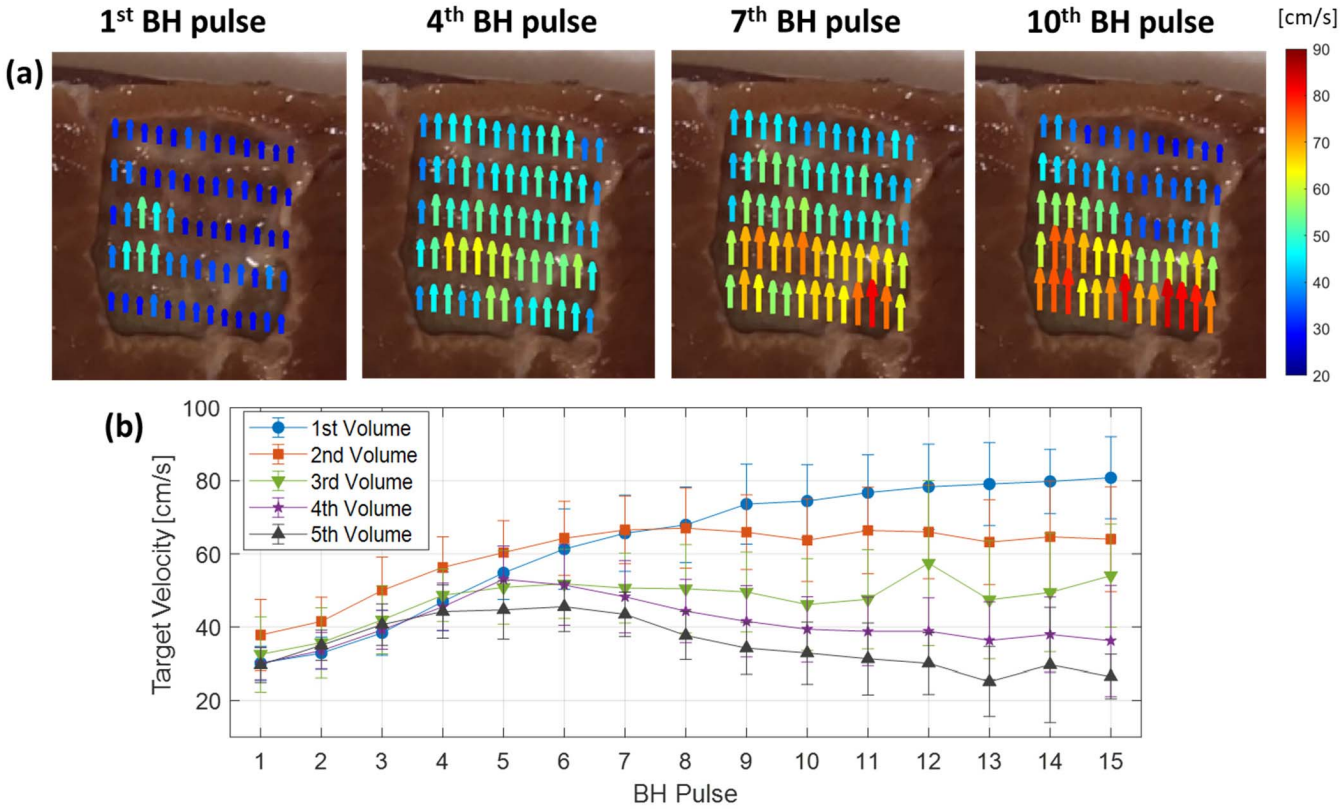


Fig. 11. (a) Target velocity map at 1 ms after a BH pulse for the first, fourth, seventh, and tenth BH pulse. The color and size of the arrows correspond to the target velocity averaged over targets that lies on the same line in the elevational direction. The position of arrows corresponds to the BH target point. Each arrow was acquired for the different number of BH pulses, but they are displayed together if the same number of BH pulses were delivered. The graph below (b) shows the target velocity averaged in all targets with respect to the BH pulse. Error bars correspond to the standard deviation.

to $v_{\max,t=1}$ in the elemental-volume treatment. Specifically, it starts from 30 cm/s, gradually increases, and then saturates around 80 cm/s. The other lines saturate or decline due to the interaction with the preexisting lesion. In general, these shifts in trend begin around the fifth BH pulse.

## IV. Discussion and Conclusion

In this study, we investigated tissue motion during BH treatment using high PRF color Doppler imaging with the ultimate goal of identifying quantitative metrics of liquefaction progression and treatment completion. The experiments were performed in progressively more complex scenarios: (1) a single BH target in the two limiting cases of the target medium—liquid blood and intact soft tissue without liquefaction; (2) an elemental-volume BH treatment with 65 BH targets; and (3) a composite-volume BH treatment with five adjacent and merging elemental-volume treatments equidistantly distributed in the axial direction.

The experiments with liquid blood showed that a BH pulse results in streaming in wave propagation direction at the focal region of the HIFU beam, with velocities dependent on the focal pressures. Conversely, intact soft tissue moves toward the HIFU transducer after a subthreshold BH pulse with a much lower velocity, consistent with the elastic rebound following axial displacement caused by acoustic radiation force.

One noteworthy observation from the BH exposures of liquid blood was that at the HIFU power sufficient to form a shock front in the focal waveform, bubbles were generated at the focus and streamed away from the transducer at much higher velocities (up to 200 cm/s). Whether the bubbles were gas or vapor bubbles or a mixture thereof was not clear, as boiling was unlikely to be achieved in liquid given the high streaming velocity of material through the focus, and shock fronts are also known to promote inertial cavitation [40], [41]. Regardless of the origin of the bubbles, this result is aligned with the findings in the early study of cavitation cloud histotripsy [25], that when the bubbles are generated, the radiation force is significantly amplified, resulting in a considerable velocity increase. Assuming that acoustic and mechanical characteristics of anticoagulated blood are similar to those of the liquefied tissue inside a BH lesion, it indicates that when tissue is liquefied at and around the HIFU focus, very high-speed streaming can be expected. This could potentially play a role in tissue disintegration, as well as serve as an indicator of treatment completion.

Tissue motion observations during BH treatment progression were qualitatively different for small (elemental) and large (composite) volume treatments. For axially small volumes, the motion was directed toward the transducer with gradually increasing and then saturating velocity as the treatment

progressed from partially to fully liquefied tissue. This motion was consistent with an elastic rebound of the tissue proximal and distally relative to the forming lesion, and the velocity was about tenfold larger than that at subthreshold BH exposures of soft tissue. We speculate that there are two contributing factors that potentiate this behavior. First, similar to the observations in liquid, when bubbles are formed in tissue at the focus, the radiation force and the corresponding tissue displacement are both increased, thus increasing the rebound velocity. Second, as the tissue at the focus becomes more and more liquefied, the streaming velocity is expected to increase and impact the distal border of the lesion, contributing to the tissue strain and subsequent rebound velocity after the BH pulse. If the HIFU focal region is axially larger than the lesion, the push imparted by radiation force will affect intact elastic tissues both proximal and distal to the liquefied lesion. In addition, in that case, the streaming motion is weak due to the insufficient distance to build up and unlikely to continue in the constrained space following the BH pulse. Indeed, in larger composite volume BH treatments, the high-speed streaming motion could only be observed when the size of the liquefied lesion was over 1 cm in the axial direction [see Fig. 9(b)-3], i.e., larger than the axial dimension of the HIFU focal lobe, which is 1.2 cm between the first nulls [28]. In these cases, neither the push induced by the radiation force nor the high-speed streaming jet reach the tissue distal to the already liquefied lesion. Therefore, the rebound motion of the distal tissue is diminished, and high-speed streaming away from the transducer within the lesion can be observed [see Fig. 9(b)-3]. Importantly, the maximum streaming velocity reached over 130 cm/s, similar to that in blood under the same acoustic conditions, and is, therefore, expected to be similar across other soft tissue types. In addition to that, the vortical flow, a low-speed reversed motion, was observed on both sides of the main streaming jet [see Fig. 9(b)-3] due to the confined volume of the lesion and the condition of continuity.

Thus, observation of streaming away from the HIFU transducer within the lesion could be a good candidate metric to ensure treatment completion in the case of large-size volumetric lesions, as it confirms the merging of the elemental treatment volumes as well.

As for candidate treatment progression metrics for smaller lesions, the maximum velocity within the whole motion-detected area ($v_{\max}$) in an elemental volume treatment was observed to grow monotonically over the treatment time. More specifically, $v_{\max}$ measured 1 ms after BH pulse ($v_{\max,t=1}$) outperformed $v_{\max}$ measured immediately after BH pulse ($v_{\max,t=0}$) in sensitivity because $v_{\max}$ is rapidly decaying within 1 ms after the 1st–4th BH pulse. In addition, the target velocity at $t = 1$ ms ($v_{\text{targ},t=1}$) defined as a maximum velocity within the target range also has a monotonical increment and saturation. Both metrics have the potential to be useful in determining tissue liquefaction in the elemental-volume BH treatments.

The aforementioned candidate metrics are not applicable to the lesions with axial sizes between those of elemental- and composite-volume lesions with $<1$ cm size: $v_{\max,t=1}$ does not represent the current treatment volume and is affected by the presence of distal liquefied volume; $v_{\text{targ},t=1}$ saturates at 5th–7th BH pulse that does not correspond to complete liquefaction; and high-speed streaming within the lesion is not observed. The axial component of $\Delta\vec{x}_{\max,t=1}$ may, however, represent a good metric in this lesion size range. This distance initially decreases with treatment time, as the location of maximum velocity shifts from a preexisting distal cavity to the current treatment volume, has a local minimum at the 4th–6th BH pulse, and then increases again and saturates after the 9th–10th BH pulses, depending on the volume position [see Fig. 10(a)]. We propose the following interpretation of this dependence. At the start of the treatment (1st–5th BH pulses), the rebound motion in the current treatment plan is consistent both qualitatively and quantitatively with that of a separate elemental volume [see Figs. 11(b) and 7(a)], and the velocity is initially lower than that in the liquefied distal cavity but is monotonically increasing until it becomes comparable. This is reflected in the decrease of $\Delta\vec{x}_{\max,t=1}$. Thereafter, the communication between the two lesion volumes–current and preexisting–starts and causes the shift of the maximum velocity distally again, hence the increase of $\Delta\vec{x}_{\max,t=1}$. Saturation of this metric could thus indicate the full merging of the lesion volumes, and thus, serve as an indicator of treatment completion. In particular, in the present case [second and third treatment volumes in Fig. 10(a)], $\Delta\vec{x}_{\max,t=1}$ saturates at 9th–10th BH pulse.

In summary, the following metrics could be considered as candidates for determining the completion of BH treatments with 10 ms long pulse depending on the axial size of the lesion.

1) Saturation of $v_{\max,t=1}$ or $v_{\text{targ},t=1}$ with respect to BH pulses for elemental-volume treatment.
2) Saturation of the axial component of $\Delta\vec{x}_{\max,t=1}$ to the value corresponding to the initial BH pulse for the small size volumetric lesion (less than the axial dimensions of the HIFU focal lobe, $<1$ cm for the current study).
3) Observing high-speed streaming motion directed away from the transducer for a large-size volumetric lesion ($>1$ cm for the current study).

Note that for ablation volumes of different sizes, one should plan on using different combinations of the above metrics.

In light of these considerations, the measurement from which the proposed metrics can be derived is the distribution of directional velocity along the HIFU propagation axis within an expanded axial range. This measurement can provide all three metrics: target velocity in the current treatment volume, maximum velocity location within the axial range, and the motion in the preexisting distal lesion. Note that such measurement does not require imaging. In fact, the SNR and spatial resolution of this measurement would be improved if the Doppler beam was in the form of a ray line, aligned with each HIFU focus location. The benefits of this approach will be investigated in future studies.

It is interesting to compare the physical mechanism of motion observed with different histotripsy methods—BH here and previously reported cavitation cloud histotripsy. In both methods, the tissue is observed to rebound after a treatment pulse, but the mechanism and dynamics of momentum transfer

to tissue are different. In BH, acoustic radiation force induced by a millisecond-long ultrasound pulse causes tissue displacement or liquid streaming away from a transducer during the pulse. Cavitation cloud histotripsy uses much shorter micro-second duration pulses that were shown to not impart significant radiation force [25]. Rather, the net motion of asymmetrically collapsing bubbles within the cloud during and after the pulses are hypothesized to cause the displacement away from the transducer [26]. After the pulse transfers the momentum to the tissue in both histotripsy methods, the tissue rebounds toward the transducer. The amount of displacement and velocities are also vastly different $-1$ cm/s for cavitation cloud histotripsy versus 30–100 cm/s for BH. Accordingly, different liquefaction metrics were proposed for the two techniques. In cavitation cloud histotripsy, the time-to-peak rebound velocity toward the transducer was found to grow and then saturate with tissue liquefaction due to progressively longer lasting bubbles. Importantly, in those studies, relatively small treatment volumes were considered (about 6 mm in size). In BH, the absolute rebound velocity rather than the time to reach it appeared to be a better metric and also potentially more practical for larger, clinically relevant treatment volumes.

This study has limitations; only a specific BH pulsing protocol (10 ms long BH pulse with PRF of 1 Hz) was used, and exposures were performed in one type of soft tissue—ex vivo bovine myocardium. We expect the BH pulselength and amplitude to affect the absolute velocity of both tissue rebound and streaming motions following BH pulses, because the momentum transfer caused by the radiation force from the HIFU pulse increases with both of these parameters. Shorter BH pulses, however, use higher amplitudes to achieve boiling within each pulse, which will have the opposite effect on absolute velocity. It is not immediately clear which effect will be dominant. We, however, expect the qualitative trends to be similar and the proposed metrics applicable to these other arrangements. Similarly, tissue homogeneity, primarily in terms of elasticity distribution, is expected to affect the absolute velocities but not the key trends—saturation of the rebound velocity and initiation of streaming with treatment progression at the corresponding target locations. Those metrics could thus serve as indicators of complete local liquefaction of inhomogeneous tissues, with the spatial resolution corresponding to the spacing of the treatment grid. These considerations will be confirmed in future studies, and the proposed metrics will be validated by correlating them to the 3-D histology of the BH lesions.

## REFERENCES


[1] T. D. Khokhlova, M. S. Canney, V. A. Khokhlova, O. A. Sapozhnikov, L. A. Crum, and M. R. Bailey, "Controlled tissue emulsification produced by high intensity focused ultrasound shock waves and millisecond boiling," *J. Acoust. Soc. Amer.*, vol. 130, pp. 3498–3510, May 2011, doi: 10.1121/1.3626152.

[2] M. S. Canney, V. A. Khokhlova, O. V. Bessonova, M. R. Bailey, and L. A. Crum, "Shock-induced heating and millisecond boiling in gels and tissue due to high intensity focused ultrasound," *Ultrasound Med. Biol.*, vol. 36, no. 2, pp. 250–267, Feb. 2010, doi: 10.1016/j.ultrasmedbio.2009.09.010.

[3] J. C. Simon, O. A. Sapozhnikov, V. A. Khokhlova, Y.-N. Wang, L. A. Crum, and M. R. Bailey, "Ultrasonic atomization of tissue and its role in tissue fractionation by high intensity focused ultrasound," *Phys. Med. Biol.*, vol. 57, no. 23, pp. 8061–8078, 2012, doi: 10.1088/0031-9155/57/23/8061.

[4] J. C. Simon, O. A. Sapozhnikov, Y.-N. Wang, V. A. Khokhlova, L. A. Crum, and M. R. Bailey, "Investigation into the mechanisms of tissue atomization by high-intensity focused ultrasound," *Ultrasound Med. Biol.*, vol. 41, no. 5, pp. 1372–1385, May 2015, doi: 10.1016/j.ultrasmedbio.2014.12.022.

[5] K. J. Pahk, S. Lee, P. Gélat, M. O. de Andrade, and N. Saffari, "The interaction of shockwaves with a vapour bubble in boiling histotripsy: The shock scattering effect," *Ultrason. Sonochem.*, vol. 70, Jan. 2021, Art. no. 105312, doi: 10.1016/j.ultsonch.2020.105312.

[6] Y.-N. Wang et al., "Mechanical decellularization of tissue volumes using boiling histotripsy," *Phys. Med. Biol.*, vol. 63, no. 23, Dec. 2018, Art. no. 235023, doi: 10.1088/1361-6560/aaef16.

[7] V. A. Khokhlova et al., "Histotripsy methods in mechanical disintegration of tissue: Towards clinical applications," *Int. J. Hyperthermia*, vol. 31, no. 2, pp. 145–162, 2015, doi: 10.3109/02656736.2015.1007538.

[8] T. D. Khokhlova et al., "Pilot in vivo studies on transcutaneous boiling histotripsy in porcine liver and kidney," *Sci. Rep.*, vol. 9, no. 1, pp.1–12, Dec. 2019, doi: 10.1038/s41598-019-56658-7.

[9] G. R. Schade, Y.-N. Wang, S. D'Andrea, J. H. Hwang, W. C. Liles, and T. D. Khokhlova, "Boiling histotripsy ablation of renal cell carcinoma in the Eker rat promotes a systemic inflammatory response," *Ultrasound Med. Biol.*, vol. 45, no. 1, pp. 137–147, Jan. 2019, doi: 10.1016/j.ultrasmedbio.2018.09.006.

[10] T. D. Khokhlova, W. L. Monsky, Y. A. Haider, A. D. Maxwell, Y. Wang, and T. J. Matula, "Histotripsy liquefaction of large hematomas," *Ultrasound Med. Biol.*, vol. 42, no. 7, pp. 1491–1498, Jul. 2016, doi: 10.1016/j.ultrasmedbio.2016.01.020.

[11] G. Nam et al., "Investigation of the potential immunological effects of boiling histotripsy for cancer treatment," *Adv. Therapeutics*, vol. 3, no. 8, Aug. 2020, Art. no. 1900214, doi: 10.1002/adtp.201900214.

[12] T. D. Khokhlova et al., "Magnetic resonance imaging of boiling induced by high intensity focused ultrasound," *J. Acoust. Soc. Amer.*, vol. 125, no. 4, pp. 2420–2431, Apr. 2009, doi: 10.1121/1.3081393.

[13] M. Hoogenboom et al., "In vivo MR guided boiling histotripsy in a mouse tumor model evaluated by MRI and histopathology," *NMR Biomed.*, vol. 29, no. 6, pp. 721–731, Jun. 2016, doi: 10.1002/nbm.3520.

[14] B. A. Rabkin, V. Zderic, and S. Vaezy, "Hyperecho in ultrasound images of HIFU therapy: Involvement of cavitation," *Ultrasound Med. Biol.*, vol. 31, no. 7, pp. 947–956, Jul. 2005, doi: 10.1016/j.ultrasmedbio.2005.03.015.

[15] M. R. Bailey et al., "Use of overpressure to assess the role of bubbles in focused ultrasound lesion shape in vitro," *Ultrasound Med. Biol.*, vol. 27, no. 5, pp. 695–708, May 2001.

[16] K. J. Pahk, M. O. de Andrade, P. Gélat, H. Kim, and N. Saffari, "Mechanical damage induced by the appearance of rectified bubble growth in a viscoelastic medium during boiling histotripsy exposure," *Ultrason. Sonochem.*, vol. 53, pp. 164–177, May 2019, doi: 10.1016/j.ultsonch.2019.01.001.

[17] A. Maxwell et al., "Disintegration of tissue using high intensity focused ultrasound: Two approaches that utilize shock waves," *Acoust. Today*, vol. 8, no. 4, pp. 24–36, 2012.

[18] T.-Y. Wang et al., "Quantitative ultrasound backscatter for pulsed cavitational ultrasound therapy-histotripsy," *IEEE Trans. Ultrason., Ferroelectr., Freq. Control*, vol. 56, no. 5, pp. 995–1005, May 2009, doi: 10.1109/TUFFC.2009.1131.

[19] T. L. Hall, J. B. Fowlkes, and C. A. Cain, "A real-time measure of cavitation induced tissue disruption by ultrasound imaging backscatter reduction," *IEEE Trans. Ultrason., Ferroelectr., Freq. Control*, vol. 54, no. 3, pp. 569–575, Mar. 2007, doi: 10.1109/TUFFC.2007.279.

[20] T.-Y. Wang, T. L. Hall, Z. Xu, J. B. Fowlkes, and C. A. Cain, "Imaging feedback of histotripsy treatments using ultrasound shear wave elastography," *IEEE Trans. Ultrason., Ferroelectr., Freq. Control*, vol. 59, no. 6, pp. 1167–1181, Jun. 2012, doi: 10.1109/TUFFC.2012.2307.

[21] T.-Y. Wang, T. L. Hall, Z. Xu, J. B. Fowlkes, and C. A. Cain, "Imaging feedback for histotripsy by characterizing dynamics of acoustic radiation force impulse (ARFI)-induced shear waves excited in a treated volume," *IEEE Trans. Ultrason., Ferroelectr., Freq. Control*, vol. 61, no. 7, pp. 1137–1151, Jul. 2014, doi: 10.1109/TUFFC.2014.3013.

[22] K. B. Bader, K. J. Haworth, A. D. Maxwell, and C. K. Holland, "Post hoc analysis of passive cavitation imaging for classification of histotripsy-induced liquefaction in vitro," *IEEE Trans. Med. Imag.*, vol. 37, no. 1, pp. 106–115, Jan. 2018, doi: 10.1109/TMI.2017.2735238.

[23] J. J. Macoskey, J. R. Sukovich, T. L. Hall, C. A. Cain, and Z. Xu, "Real-time acoustic-based feedback for histotripsy therapy," *J. Acoust. Soc. Amer.*, vol. 141, no. 5, p. 3551, 2017, doi: 10.1121/1.4987518.
[24] T. Li, T. Khokhlova, O. Sapozhnikov, M. O'Donnell, and J. Hwang, "A new active cavitation mapping technique for pulsed HIFU applications-bubble Doppler," *IEEE Trans. Ultrason., Ferroelectr., Freq. Control*, vol. 61, no. 10, pp. 1698–1708, Oct. 2014, doi: 10.1109/TUFFC.2014.006502.
[25] R. M. Miller, X. Zhang, A. D. Maxwell, C. A. Cain, and Z. Xu, "Bubble-induced color Doppler feedback for histotripsy tissue fractionation," *IEEE Trans. Ultrason., Ferroelectr., Freq. Control*, vol. 63, no. 3, pp. 408–419, Mar. 2016, doi: 10.1109/TUFFC.2016.2525859.
[26] J. J. Macoskey et al., "Bubble-induced color Doppler feedback correlates with histotripsy-induced destruction of structural components in liver tissue," *Ultrasound Med. Biol.*, vol. 44, no. 3, pp. 602–612, 2018, doi: 10.1016/j.ultrasmedbio.2017.11.012.
[27] X. Zhang et al., "Real-time feedback of histotripsy thrombolysis using bubble-induced color Doppler," *Ultrasound Med. Biol.*, vol. 41, no. 5, pp. 1386–1401, May 2015, doi: 10.1016/j.ultrasmedbio.2014.12.006.
[28] C. R. Bawiec et al., "A prototype therapy system for boiling histotripsy in abdominal targets based on a 256-element spiral array," *IEEE Trans. Ultrason., Ferroelectr., Freq. Control*, vol. 68, no. 5, pp. 1496–1510, May 2021, doi: 10.1109/TUFFC.2020.3036580.
[29] T. D. Khokhlova, Y. A. Haider, A. D. Maxwell, W. Kreider, M. R. Bailey, and V. A. Khokhlova, "Dependence of boiling histotripsy treatment efficiency on HIFU frequency and focal pressure levels," *Ultrasound Med. Biol.*, vol. 43, no. 9, pp. 1975–1985, Sep. 2017, doi: 10.1016/j.ultrasmedbio.2017.04.030.
[30] P. V. Yuldashev, M. M. Karzova, W. Kreider, P. B. Rosnitskiy, O. A. Sapozhnikov, and V. A. Khokhlova, "'HIFU beam:' A simulator for predicting axially symmetric nonlinear acoustic fields generated by focused transducers in a layered medium," *IEEE Trans. Ultrason., Ferroelectr., Freq. Control*, vol. 68, no. 9, pp. 2837–2852, Sep. 2021, doi: 10.1109/TUFFC.2021.3074611.
[31] P. A. Hasgall et al., "It 'is database for thermal and electromagnetic parameters of biological tissues," Version 4.0, IT'IS Found., Zürich, Switzerland, Tech. Rep., May 15, 2018, [Online]. Available: https://itis.swiss/database, doi: 10.13099/VIP21000-04-0.
[32] D. H. Evans and W. N. McDicken, *Doppler Ultrasound: Physics Instrumentation and Clinical Applications*. Hoboken, NJ, USA: Wiley, 1989.
[33] S. Bjærum, H. Torp, and K. Kristoffersen, "Clutter filter design for ultrasound color flow imaging," *IEEE Trans. Ultrason., Ferroelectr., Freq. Control*, vol. 49, no. 2, pp. 204–216, Feb. 2002, doi: 10.1109/58.985705.
[34] C. Kasai, K. Namekawa, A. Koyano, and R. Omoto, "Real-time two-dimensional blood flow imaging using an autocorrelation technique," *IEEE Trans. Sonics Ultrason.*, vol. SU-32, no. 3, pp. 458–464, May 1985.
[35] V. G. Andreev, V. N. Dmitriev, Y. A. Pishchal'nikov, O. V. Rudenko, O. A. Sapozhnikov, and A. P. Sarvazyan, "Observation of shear waves excited by focused ultrasound in a rubber-like medium," *Acoust. Phys.*, vol. 43, no. 2, pp. 123–128, 1997.
[36] Y. A. Pishchalnikov, O. A. Sapozhnikov, and T. V. Sinilo, "Increase in the efficiency of the shear wave generation in gelatin due to the nonlinear absorption of a focused ultrasonic beam," *Acoust. Phys.*, vol. 48, no. 2, pp. 214–219, Mar. 2002.
[37] M. A. Ghanem et al., "Field characterization and compensation of vibrational nonuniformity for a 256-element focused ultrasound phased array," *IEEE Trans. Ultrason., Ferroelectr., Freq. Control*, vol. 65, no. 9, pp. 1618–1630, Sep. 2018, doi: 10.1109/TUFFC.2018.2851188.
[38] S. Chien, S. Usami, R. J. Dellenback, M. I. Gregersen, L. B. Nanninga, and M. M. Guest, "Blood viscosity: Influence of erythrocyte aggregation," *Science*, vol. 157, no. 3790, pp. 829–831, Aug. 1967.
[39] G. P. L. Thomas, T. D. Khokhlova, and V. A. Khokhlova, "Partial respiratory motion compensation for abdominal extracorporeal boiling histotripsy treatments with a robotic arm," *IEEE Trans. Ultrason., Ferroelectr., Freq. Control*, vol. 68, no. 9, pp. 2861–2870, Sep. 2021, doi: 10.1109/TUFFC.2021.3075938.
[40] A. D. Maxwell et al., "Cavitation clouds created by shock scattering from bubbles during histotripsy," *J. Acoust. Soc. Amer.*, vol. 130, no. 4, pp. 1888–1898, Oct. 2011, doi: 10.1121/1.3625239.
[41] C. R. Bawiec et al., "Inertial cavitation behaviors induced by nonlinear focused ultrasound pulses," *IEEE Trans. Ultrason., Ferroelectr., Freq. Control*, vol. 68, no. 9, pp. 2884–2895, Sep. 2021, doi: 10.1109/TUFFC.2021.3073347.

**Minho Song** (Graduate Student Member, IEEE) received the B.S. and M.S. degrees in mechanical engineering from Yonsei University, Seoul, South Korea, in 2013 and 2015, respectively. He is currently pursuing the Ph.D. degree in mechanical engineering with the University of Washington, Seattle, WA, USA.

Before starting his Ph.D. program, he was a Noise and Vibration Research Engineer with Korea Aerospace Industries, Sacheon, South Korea, from 2015 to 2019. His research interests include in the field of biomedical and nonlinear acoustics, including ultrasound imaging guidance in cavitation-based ultrasound therapy such as boiling histotripsy (BH) and drug delivery.

**Gilles P. L. Thomas** received the Engineering degree in general engineering from the École Centrale de Nantes, Nantes, France, in 2014, the Engineering degree in mechatronics engineering and the M.S. degree in control and automation engineering from the Polytechnic School, University of São Paulo, São Paulo, Brazil, in 2014 and 2015, respectively, and the Ph.D. degree in biomedical engineering from the Université Lyon 1, Lyon, France, in 2019.

He is currently with the Applied Physics Laboratory, University of Washington, Seattle, WA, USA, for postdoctoral training.

**Vera A. Khokhlova** received the M.S. degree in physics and the Ph.D. and D.Sc. degrees in acoustics from Moscow State University (MSU), Moscow, Russia, in 1986, 1991, and 2012, respectively.

She is currently an Associate Professor with the Department of Acoustics, Physics Faculty, MSU. Since 1995, she has been with the Center for Industrial and Medical Ultrasound, Applied Physics Laboratory, University of Washington, Seattle, WA, USA. Her research interests include the field of nonlinear acoustics, therapeutic ultrasound, including metrology and bioeffects of high intensity focused ultrasound (HIFU) fields, shock wave focusing, nonlinear wave propagation in inhomogeneous media, and nonlinear modeling.

Dr. Khokhlova has been a fellow since 2008 and has served as a member for the Executive Council of the Acoustical Society of America from 2012 to 2015, the Board of the International Society for Therapeutic Ultrasound from 2004 to 2008 and from 2011 to 2014, and the "Physical Ultrasound" Division of the Scientific Council on Acoustics of the Russian Academy of Sciences since 2009. She has been an Associate Editor of the IEEE TRANSACTIONS ON ULTRASONICS, FERROELECTRICS, AND FREQUENCY CONTROL since 2013.

**Oleg A. Sapozhnikov** received the M.S. degree in physics, and the Ph.D. and D.Sc. degrees in acoustics from Moscow State University (MSU), Moscow, Russia, in 1985, 1988, and 2008, respectively.

Since 1996, he has been with the Applied Physics Laboratory, Center for Industrial and Medical Ultrasound, University of Washington, Seattle, WA, USA. He is currently a Professor with the Department of Acoustics, Physics Faculty, MSU. His research interests include fields of physical acoustics, nonlinear wave phenomena, medical ultrasound, including shock wave lithotripsy, high intensity focused ultrasound (HIFU), and ultrasound-based imaging.

Dr. Sapozhnikov has been a member of the International Society for Therapeutic Ultrasound since 2001, a member of the Board of the International Congress on Ultrasonics since 2008, and the Head of the "Physical Ultrasound" Division of the Scientific Council on Acoustics of the Russian Academy of Sciences since 2009. He has been a fellow of the Acoustical Society of America since 2009. He was a recipient of the M.V. Lomonosov Prize in Physics in 1991, the Prize of the European Academy for Young Russian Scientists in 1994, and the Early Career Award of the International Commission for Acoustics in 2004.

**Michael R. Bailey** received the B.S. degree in mechanical engineering from Yale University, New Haven, CT, USA, in 1991, and the M.S. and Ph.D. degrees in mechanical engineering from the University of Texas at Austin, Austin, TX, USA, in 1994 and 1997, respectively.

He is currently a Senior Principal Engineer with the Applied Physics Laboratory and a Professor of Mechanical Engineering and an Adjunct Professor of urology with the University of Washington, Seattle, WA, USA. His research interests include cavitation, lithotripsy, high intensity focused ultrasound (HIFU), and ultrasound imaging; currently his energy is focused on developing ultrasound-based technology to break and reposition kidney stones.

Dr. Bailey has been a fellow of the Acoustical Society of America (ASA) since 2007 and served for the ASA Executive Council from 2014 to 2017, the Board of the International Society for Therapeutic Ultrasound (ISTU) from 2009 to 2012, the Bioeffects Committee of the American Institute for Ultrasound in Medicine from 2006 to 2012, and the Biomedical Acoustics Technical Committee of the ASA as the Chair from 2005 to 2008. He received Early Career Award from ASA in 2004 and ISTU in 2008.

**Adam D. Maxwell** received the B.S. degree in electrical engineering from the University of Washington, Seattle, WA, USA, in 2006, and the M.S. degree in electrical engineering and the Ph.D. degree in biomedical engineering from the University of Michigan, Ann Arbor, MI, USA, in 2007 and 2012, respectively.

From 2012 to 2014, he was a Postdoctoral Fellow with the Department of Urology, University of Washington, where he is currently an Acting Assistant Professor. His research interests include the development of image-guided ultrasound therapies, including focused ultrasound for mechanical tissue ablation (histotripsy) and lithotripsy.

**Petr V. Yuldashev** received the M.S. degree in physics and the Ph.D. degree in acoustics from Moscow State University (MSU), Moscow, Russia, in 2008 and 2011, respectively, and the Ph.D. degree in acoustics from École Centrale de Lyon (ECL), Ecully, France, according to the double Ph.D. program of the French Government.

After graduation from the Ph.D. program, he was appointed by Moscow State University and currently is an Associate Professor with the Department of General Physics and Condensed Matter Physics, Physics Faculty, MSU. He is also with the Department of Fluid Mechanics, Acoustics, and Energetics, ECL, to work on the propagation of shock waves in a turbulent atmosphere and the utilization of nonlinear acoustics effects to calibrate high-frequency broadband microphones. His research interests pertain to nonlinear acoustics, shock wave focusing, nonlinear wave propagation in inhomogeneous media, sonic booms, nonlinear modeling, and shadowgraphy measurement methods for acoustic phenomena.

**Tatiana D. Khokhlova** (Member, IEEE) received the Ph.D. degree in physics from Moscow State University (MSU), Moscow, Russia, in 2008.

She was with the Applied Physics Laboratory, University of Washington (UW), Seattle, WA, USA, for postdoctoral training, and then completed a Research Fellowship with the Department of Medicine, UW, where she is currently a Research Assistant Professor. Her research interests include physical acoustics, therapeutic ultrasound, and photoacoustic imaging.